Contents lists available at ScienceDirect

Electrochimica Acta

journal homepage: www.elsevier.com/locate/electacta

Polyborosilazane derived ceramics - Nitrogen sulfur dual doped graphene nanocomposite anode for enhanced lithium ion batteries

Muhammad Idrees [a], Saima Batool [a], Jie Kong [a, **], Qiang Zhuang [a], Hu Liu [b, c], Qian Shao [d], Na Lu [e], Yining Feng [e], Evan K. Wujcik [f], Qiang Gao [i], Tao Ding [g, ***], Renbo Wei [h, ****], Zhanhu Guo [b, *]

[a] MOE Key Laboratory of Space Applied Physics & Chemistry, Shaanxi Key Laboratory of Macromolecular Science &Technology, School of Natural & Applied Sciences, Northwestern Polytechnical University, Xi'an, 710072, China
[b] Integrated Composites Laboratory (ICL), Department of Chemical & Biomolecular Engineering, University of Tennessee, Knoxville, TN, 37996, USA
[c] Key Laboratory of Materials Processing and Mold (Zhengzhou University), Ministry of Education, National Engineering Research Center for Advanced Polymer Processing Technology, Zhengzhou University, Zhengzhou, 450002, China
[d] College of Chemical and Environmental Engineering, Shandong University of Science and Technology, Qingdao, 266590, China
[e] Lyles School of Civil Engineering, School of Materials Engineering, Birck Nanotechnology Center, Purdue University, West Lafayette, IN, 47906, USA
[f] Materials Engineering and Nanosensor [MEAN] Laboratory, Department of Chemical and Biological Engineering, The University of Alabama, Tuscaloosa, USA
[g] College of Chemistry and Chemical Engineering, Henan University, Kaifeng, 475004, China
[h] Research Branch of Advanced Functional Materials, School of Materials and Energy, University of Electronic Science and Technology of China, Chengdu, 611731, China
[i] Center for Nanophase Materials Sciences, Oak Ridge National Laboratory, P.O. Box 2008, Oak Ridge, TN, 37831, USA

ARTICLE INFO

ABSTRACT

Silicon boron carbon nitride ceramic nanocomposites filled with nitrogen sulfur dual-doped graphene sheets (SiBCN/NSGs) were designed and synthesized by inserting pyrolyzed NSGs into the polymer derived SiBCN via ball ball milling technique and their feasibility to serve as lithium ion battery anode was tested. The insertion of NSGs in SiBCN caused extrinsic defects and more active sites, both increased the lithiation and anode stability. The resulting material significantly improved the Li-ion loading capacity and gave a higher rate ability. The high cycling performances were attributed to the stacked graphene sheets of NSGs and increased disordered carbon sites (amorphous structure), such as rearrangement of -sp^2 carbon chains and formation of B(C)N domains of polymer derived ceramic (PDC). The NSGs generated extrinsic defects and more active sites, hence promoted the electrode performance. The nanocomposites exhibited a reversible capacity of 785 mAh g^{-1} even at a high current density of 450 mA g^{-1} over 800 cycles, representing a high retained capacity of ~780 mAh g^{-1} with an average decay of 0.006% per cycle. Furthermore, the SiBCN anode revealed a charge capacity of 365 mAh g^{-1} at 450 mA g^{-1} after 500 cycles, indicating that both the assembled anodes have potential practical applications in lithium-ion batteries.

© 2018 Elsevier Ltd. All rights reserved.

1. Introduction

Lithium ion batteries (LIBs) are needed for handy electronic devices [1]. The commercially available graphite anode has a limited specific capacity of ~370 mAh g^{-1} at 100 mA g^{-1} [2]. Numerous precursors with modified structure have been investigated to obtain high performance anode materials, of which the silicon based anode materials are promising alternatives due to their high theoretical capacity of ~4200 mAh g^{-1} for LIBs [3,4]. Although substantial pulverization of silicon based anodes can destroy the initially formed solid electrolyte interface (SEI), the capacity is still degraded because of 400% volume expansion during charging and discharging process [5]. This fast capacity fading is

attributed to the loss of electrical conductivity and the cracked surface from breaking the formed SEI, which cause the depletion of excess Li-ions and electrolyte [6,7]. For large size battery application, the degradation of electrochemical performance during delithiation makes Si based anodes incompetent. Therefore, tremendous efforts have been made to improve the anode performance of LIBs. The Si based polymer derived ceramics (PDCs) have been recognized as advanced anode materials due to their disordered structure, which strongly depends on the pyrolyzing conditions. These disordered PDCs prepared via pyrolyzed precursor exhibited exclusive amorphous structure, resistance to oxidation, high thermal stability and having impressive electrical properties [8–12]. These significant features of PDCs are responsible for high performance in LIBs. They have good ability to store lithium ions compared to conventional graphite anodes [13–17].

In addition, nitrogen sulfur dual-doped graphene sheet (NSGs) can enhance electrochemical performance of PDC since the Li-ion storage ability strongly depends on the anode structural material [18]. The improved electrochemical properties in the energy storage devices were attributed to the synergistic effects of doped heteroatoms in the stacked graphene [19]. Two synthetic routes were used for the modification of stacked graphene. One is the post-treatment of stacked graphene precursor with reactive heteroatom sources e.g. borane, ammonia, ionic liquids and triphenylphosphine [20–25]. The other is the pyrolysis of the mixed stacked graphene and heteroatom to directly dope heteroatoms into carbon backbone [22]. This gives a limited performance in LIBs due to its inevitable agglomeration. However, an effective mechanism of dual-doped N/S heteroatoms is proposed for the improved electrochemical performance of LIBs.

The heteroatom doping influences the wettability of the pyrolyzed carbonaceous materials, which increases the super capacitive performance [26,27]. The reported studies suggested that the electrochemical performance of the LIBs can be highly enhanced by doping various existential forms of carbon. For example, Xu and coworkers [28] synthesized a nitrogen-doped carbon/graphene hybrid material, which exhibited a good sodium storage performance due to the influence of N atoms. Zhang et al. [29] prepared 2D porous N-doped carbon sheets via chemical activation of polypyrrole (PPy)-functionalized graphene with KOH, and showed an improved electrochemical performance. The SiBCN ceramic has also been evaluated as anode materials for LIBs. However, pure PDC anode materials gave low electrochemical performance. The N and S increased the defects and active sites for lithium ion insertion [30]. The ball milling increased the specific surface area and enhanced the extrinsic defects and active sites. The broad interlayer distance of carbon enhanced the Li-storage capacity and high rate capability [31]. In addition; the heteroatom doping can also create a pseudo-capacitance due to a better surface interaction between the electrolyte and dopant species [32]. Moreover, the enhanced performance of the composites was ascribed to the amorphous structure such as rearrangement of $-sp^2$ carbon chains and formation of B(C)N domains. Meanwhile, the electrochemical performance of SiBCN/NSGs composites prepared via ball milling has not been investigated yet.

In the present work, SiBCN/NSGs derived ceramics nanocomposites were prepared by the insertion of pyrolyzed NSGs into the polymer derived SiBCN via ball milling. The amorphous structure of SiBCN and the existential form of NSGs in the nanocomposites under different temperatures were analysed. The amorphous structure of SiBCN led to effective lithium ion storage whereas the insertion of NSGs into PDC composites enhanced the conductivity. The structure of active anode nanocomposites pyrolyzed at different temperatures was investigated by FTIR, XRD and Raman spectroscopy. Benefiting from the structural characteristics

and synergistic effects of N and S dual doping, the resultant nanocomposites presented to be a versatile anode active material for LIBs in terms of good reversible capacity of ~780 mAh g^{-1} at 450 mA g^{-1} with stable rate performance, as well as prolonged cycling life. Dual doped NSGs with extrinsic defects and more active sites were disclosed to enhance the electrochemical performances with PDC nanocomposites serving as a conduction source simultaneously while serving as the LIBs anode.

2. Experimental section

2.1. Materials

Boron trichloride (BCl$_3$), dichloromethylsilane (MeHSiCl$_2$), diphenyldichlorosilane (C$_6$H$_5$)$_2$Cl$_2$Si and hexamethyldisilazane (HMDZ, CH$_3$)$_3$SiNHSi (CH$_3$)$_3$ were purchased from Tokyo Chemical Industry Co. Ltd., Japan and Sigma-Aldrich. The 2, 5-dimercapto-1, 3, 4-thiadiazol (DMcT, C$_2$H$_2$N$_2$S$_3$), hexa decyltrimethyl-ammonium bromide (CTAB, CH$_3$ (CH$_2$)$_{15}$N (Br) (CH$_3$)$_3$) and ammonium persulfate (APS, (NH$_4$)$_2$S$_2$O$_8$) were purchased from Tianjin Heowns and Sigma-Aldrich respectively. All the commercially available chemical reagents were used as received without any purification.

2.2. Synthesis of polyborosilazane

Polyborosilazane was synthesized under argon atmosphere according to the reported procedures [33] as shown in Scheme S1. Briefly, BCl$_3$ (50 mL) was added into a 250 mL dried vacuum three-necked flask equipped with a mechanical stirrer and an argon inlet, and cooled down to −78 °C. Under argon flow, the three-necked flask was added subsequently with MeHSiCl$_2$ (5.87 g), (C$_6$H$_5$)$_2$Cl$_2$Si (13.05 g) and (CH$_3$)$_3$SiNHSi (CH$_3$)$_3$ (40.35 g) slowly through syringe with a molar ratio of (1: 1: 1: 4.9). When the three-necked flask was cooled down to room temperature under continuous stirring, the temperature was maintained at 60 °C for 1–2 h first and 100 °C for next 2 h, then increased the temperature to 250 °C at a rate of 10 °C per 10 min and kept 250 °C at for 3–4 h. Finally, the solvent was removed under vacuum, yielding viscous translucent oil.

2.3. Synthesis of nitrogen sulfur dual doped graphene sheets

First, the stacked graphene was prepared from natural graphite using a modified Hummers procedure [34]. A solution of 0.3 g C$_2$H$_2$N$_2$S$_3$ was dissolved in 20 mL CH$_3$OH. Then, the mixed solution was added into the flask containing 10 g (8 mg L^{-1}) stacked graphene solution. In addition, 0.1 g CTAB was subsequently added under constant stirring. Then, the mixed solution of CH$_3$OH/H$_2$O (10 mL, 1:1 by volume) containing 1.37 g (NH$_4$)$_2$S$_2$O$_8$ was added dropwise into the above solution. After stirring at room temperature for 24 h, the mixture was filtered off, washed with CH$_3$OH/H$_2$O, and then dried at 80 °C under vacuum.

2.4. Ceramic transformation

The as-synthesized polyborosilazane (2.5 g) and NSGs (2.5 g) were heat treated in a tubular furnace (GSL-1700X, Kejing New Mater. Ltd., China) separately with an argon gas stream. Initially, the cross-linking was carried out at 200 °C (heating rate: 2 °C/min, holding time: 2 h) followed by heat treatment at 600–1000 °C (heating rate: 2 °C/min, holding time: 2 h) under an argon stream. Afterward, the SiBCN (P1) and NSGs (P2) ceramics were ball milled, sieved down to 100 μm powders and named as C1-C3 and C4-C6. For composites (P3), the stoichiometric amount of pyrolyzed ceramic P1 (0.4 g) and P2 (0.04 g) at various temperatures was also

ball milled (Across International LLC, USA) separately into powders with 10: 1 ratio each under 300 rpm for 4 h and then sieved through a 100 μm mesh and labelled as C2/C5-C3/C5 nano-composites, respectively. Fig. 1 shows the synthesis of dual-doped NSGs and the proposed synthesis mechanism with SiBCN ceramic.

The electrode was prepared using 80 wt% active material, 10 wt% acetylene black (Super P® (Timcal Ltd., Switzerland) and 10 wt% polyvinylidene difluoride (PVDF, MW: ~800,000 g mol^{-1}, HSV 900, Power source battery sales department, Taiyuan, China) with a ratio of 8:1:1 that were mixed in N-*methyl* pyrrolidinone (NMP, BASF, Germany) to obtain a slurry. Then, the slurry was cast on a 15 μm thick copper foil (SE-Cu58, Schlenk Metallfolien, Germany) via a 10 μm doctor edge. The active material loading level and density of anode in this work were 1.34 mg cm^{-2} and 1.1854 mg cm^{-3}. The coated foil was desiccated at 120 °C for 24 h under Buchi vacuum oven to evaporate the solvent. Lithium metal foil with 0.47 mm (470 μm) thickness (99.9% purity, Alfa Aesar, China), Celgard 2400, and 1 mL lithium hexafluorophosphate (LiPF$_6$) in EC: DMC (ratio 1:1, Alfa Aesar, China) were used as the counter electrode, separator and electrolyte, respectively. Finally, the LIR 2025 coin-type cells were assembled and crimped at 5 MPa in an Ar filled glove box Super (1220/750/900 Mikrouna, China H$_2$O < 0.01 ppm, O$_2$ < 0.01 ppm).

2.5. Characterization

All the synthesis was carried out under inert conditions, using standard schlenk techniques. Thermogravimetric analyzer (TGA, CH STA449F3, Netzsch, Germany) was carried out under argon atmosphere (gas flow 50 mLmin^{-1}) at a heating rate of 10 °C min^{-1}. A Fourier transform infra-red spectrum (IR) was recorded using a spectrophotometer (Perkin Elmer 781, USA). The crystallographic pattern of specimens was collected using a powder X-ray diffractometer (XRD, Rigaku D/Max-2550VB+/PC) with Cu Kα radiation at an angle pause of 10°-90° with a calculating time of 0.5 s/ 0.02° step. Raman spectra for interpenetrating ceramic network was obtained with 514 nm Ar$^+$ laser (Jobin Yvon Labor Raman HR-800 spectrometer). The elemental identification of ceramic and the heteroatom functional group distribution measurement were acquired via a PHI Quantera SXM with Al Kα excitation. The curve fitting of the XPS spectra was performed using the shirely method.

Scanning electron microscopy (SEM) morphology was observed using a VEGA3XMH instrument (Tescan Co., Czech Republic). A variable pressure electron microscope equipped with oxford energy dispersive X-ray spectrometer was employed to obtain the elemental composition of the as-prepared anode specimens. The structures of anode materials were characterized by transmission electron microscopy (TEM, JEOL JEM-ARM200F).

The LIR 2025 coin type cells were used during the test analyses. The galvanostatic profiles, rate capability and cells cycling presentation were examined using a LANHE CT2001A (Wuhan, China) in a voltage range of 0.01-1.0 V and 0.1–3.0 V vs Li/Li$^+$. The cyclic voltammetry (CV) performance was recorded on a Princeton chemical workstation (PARSTATMC-500, USA) in the potential range of 0.01−3.0 V vs Li/Li$^+$ with a sweep rate of 0.04 mV s^{-1}. All the electrochemical testes were carried out at 25 °C.

3. Results and discussion

The transformation of polyborosilazane and dual-doped NSGs into ceramic was analysed by TGA under Ar [35]. The synthesized precursor and additive endured a hasty thermal degradation ranging from 150 to 350 °C for polyborosilazane. This weight thermolysis was mainly accompanied by the evolution of H$_2$O and CO, which was caused by the oxidation of methyl groups, CH$_4$ and H$_2$ during pyrolysis. The sharp weight loss in the temperature range
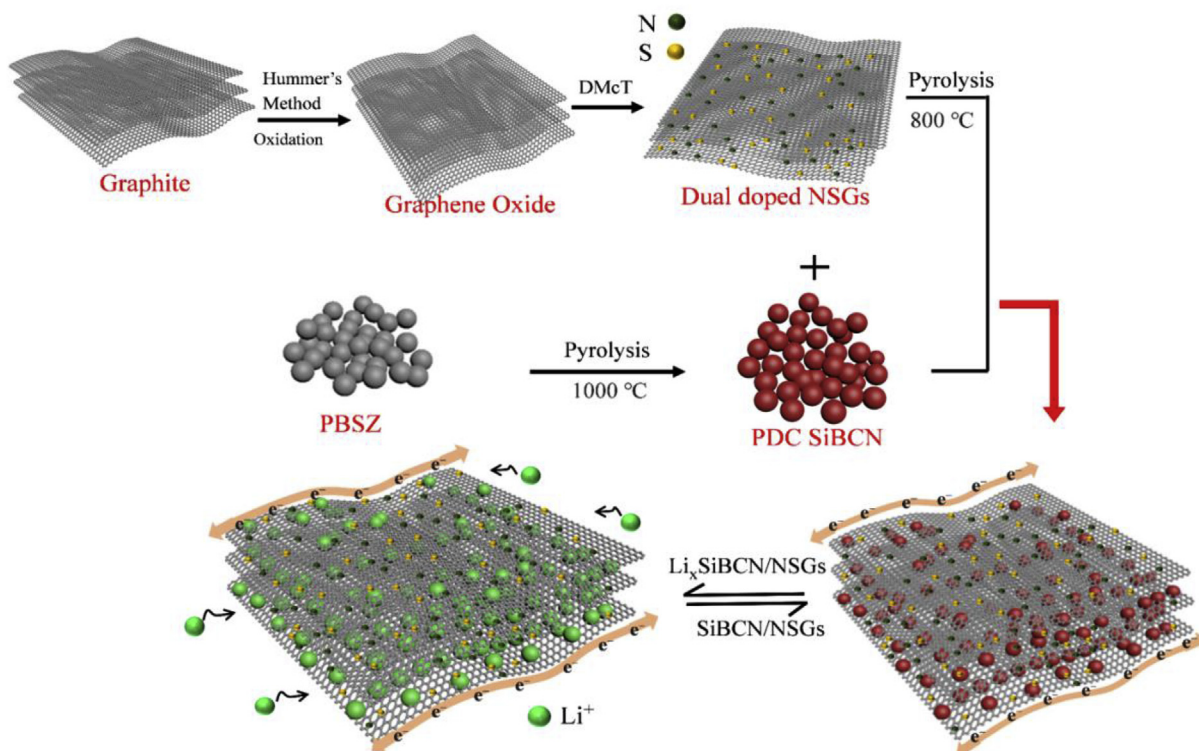
Fig. 1. Schematic representing the charge/discharge mechanism of derived ceramic nanocomposites. Bulk discharge occurs via adsorption at amorphous carbon phase, which is distributed in the SiBCN matrix. Large dual-doped NSGs serve as an efficient electron conductor and flexible support.

of 200–290 °C for NSGs resulted from its nitrogen and sulfur containing groups, and followed by decarboxylation and elimination of hydroxyl functionalities [36]. The curves were nearly smoothed off above 350 °C for polyborosilazane and 200–290 °C for NSGs, Fig. 2a. The polyborosilazane with low cross linking density and molecular weight could volatilize out at the beginning of the pyrolysis process which results in low ceramic yield and a great weight loss. The results showed that polyborosilazane and NSGs were stable at 450 and 800 °C, suggesting a stable ceramic material above 600 °C [37].

The chemical evolution during the pyrolysis was also corroborated via FTIR analysis. Fig. 2b shows the FTIR spectra of as-prepared anode specimens. From C1 to C3 anode specimens, the peak of N-H (3388 cm^{-1}) sharply decreased. While the Si-H (2366 cm^{-1}) peak was evidently weakened below 600 °C and completely disappeared at selected temperatures. The dehydrogenation coupling and transformation of Si-H/Si-H and N-H took place mainly [38], as shown in Equations (1) and (2). The intensity of the peak at 2935-3052 cm^{-1} was gradually reduced at 1000 °C, specifying that the decomposition of aliphatic C-H$_x$ was completed at 1000 °C. From C2/C5-C3/C5 anode specimens, the peaks at 3401.3, and 1319.8 cm^{-1} were ascribed to the stretching vibration of N-H and Si-CH$_3$ for the nanocomposites, and disappeared at higher temperature arising from the decomposition of organic lateral groups (C/H), which contributed to the amorphous nature of silicon boron carbon nitride. The involved C=C in the hydroboration reaction also decreased with increasing the temperature. Only one broad peak was retained at 600 °C for C1 and C2/C5 anode specimens, other peaks from organic groups almost disappeared. This indicated that the transformation from polymer to ceramic was completed at elevated temperatures [39]. It was also observed that at a higher temperature, the spectra of samples heated at 800 and 1000 °C were parallel. The spectra showed amorphous nanocomposites that might contain B-N, C-C, Si-C and Si-N bonds [40–43]. Furthermore, the chemical evolution during the pyrolysis of NSGs approached to ceramic (see Fig. S3a in the supporting information).
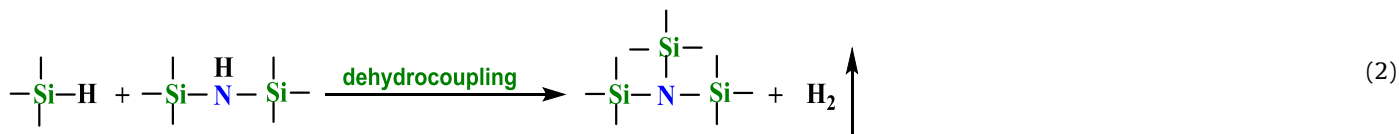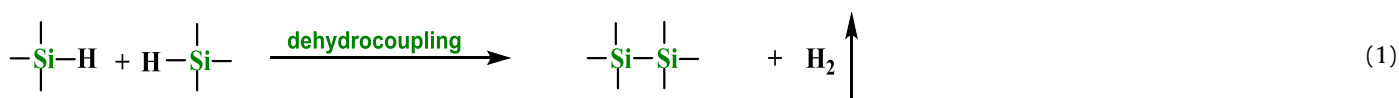
nanocomposite anode materials were still highly disordered as shown in Fig. S2. The large number of amorphous carbon observed in TEM analysis verified a lower crystallinity. For HRTEM analysis of dual-doped NSGs (see the supporting information, Figs. S1d–f (ESI), the results were consistent with the EDS and XPS analyses (Fig. 4, Fig. S3b). The h-BN phase was observed with the diffraction planes (002, 101) [44]. The higher temperature may contribute to the partial crystallization of Si$_3$N$_4$, SiC and beta-SiC [45–47], implying that boron can effectively enhance the temperature resistance and crystallization.

Raman spectroscopy was employed to determine the structural features of carbon phase in anode materials. Fig. 2d shows the comparison for the characteristic bands of C1-C3 and C2/C5-C3/C5 nanocomposite anode materials pyrolyzed at different temperatures. The distinct peaks corresponded to the D and G band of C1-C3 and C2/C5-C3/C5 nanocomposite anode materials, respectively. For the C1-C3 and C2/C5-C3/C5 nanocomposite anode materials, the D band, represented the disorder-induced vibration mode of lamellar layer in carbon phase, was associated with the sp^2 hybridization, while the G band mode corresponded to the in-plane sp^2-hybridized carbon atoms (bond stretching). This indicated that the sample contains disordered, linear carbon chain and sp^2 carbon. The relative intensity ratios of I_D/I_G were 1.09 and 1.2 for C3 and C3/C5 nanocomposite anode materials, respectively. The increases in the integrated intensity ratio at higher temperature for both anode materials were due to the existence of defects. The observed higher intensity ratio indicated more defects for the C3/C5 nanocomposite anode material compared to other anode materials. This increased defect was due to the insertion of NSGs ceramic into SiBCN. This type of dual-doped carbon surfaces offered more sites for the insertion and extraction of Li ions.

The chemical bonding of ceramic anodes materials was further examined by X-ray photoelectron spectroscopy. The chemical states of all the materials are shown in Fig. 3 and Fig. S3b). The presence of oxygen for the XPS survey spectrum was from the hydrolysis of SiBCN during pyrolysis. The presence of S2p and N1s at 150 and 400 eV in the XPS spectrum suggested that sulfur and ni-

$$-\overset{|}{\underset{|}{Si}}-H \;+\; H-\overset{|}{\underset{|}{Si}}- \quad\xrightarrow{\text{dehydrocoupling}}\quad -\overset{|}{\underset{|}{Si}}-\overset{|}{\underset{|}{Si}}- \quad+\quad H_2\uparrow \tag{1}$$

$$-\overset{|}{\underset{|}{Si}}-H \;+\; -\overset{|}{\underset{|}{Si}}-\overset{H}{\underset{|}{N}}-\overset{|}{\underset{|}{Si}}- \quad\xrightarrow{\text{dehydrocoupling}}\quad -\overset{|}{\underset{|}{Si}}-\overset{-\overset{|}{\underset{|}{Si}}-}{\underset{|}{N}}-\overset{|}{\underset{|}{Si}}- \quad+\quad H_2\uparrow \tag{2}$$

Fig. 2c shows the powder XRD patterns of the as-prepared C1-C3 anode materials. The XRD results suggested that C1-C3 anode materials were amorphous when it was heated at 600–1000 °C. This could be concluded from the prominent broad hump ranging from 2θ = 17°-23° (002) and 44° (101). The nanocomposites produced at higher temperature have a good transition of Si/C phase and have a disordered structure. This disordered structure could be ascribed to the stacked layers of dual-doped NSGs (see the supporting information for C4-C6 anode materials (Fig. S4). The HRTEM analysis further demonstrated that the C3 and C3/C5

trogen elements had been effectively merged into the SiBCN. The elemental content ratios are listed in Table 1. In order to understand the chemical states in C3/C5 nanocomposite anode material, high resolution B1s, N1s, Si2p, S2p and C1s were deconvoluted into different peaks (Fig. 3). The peak at 191.2 eV was assigned to B-N, which was consistent with the FTIR analyses. Other deconvoluted peaks at 190.3, 189.7, and 191.9 eV (Fig. 3g) belonged to the B-B, B-C and B-O bond, respectively. The peaks at 101.4, 102.6 and 103.6 eV for Si2p shown in Fig. 3e were ascribed to the Si-C and Si-N bonds. In Fig. 3c, the peaks at 397.9, 399.3 and 401 eV were assigned to the N1s of C-C and Si-C bond. The peaks at 530.3, 532.3 and 533.9 eV in
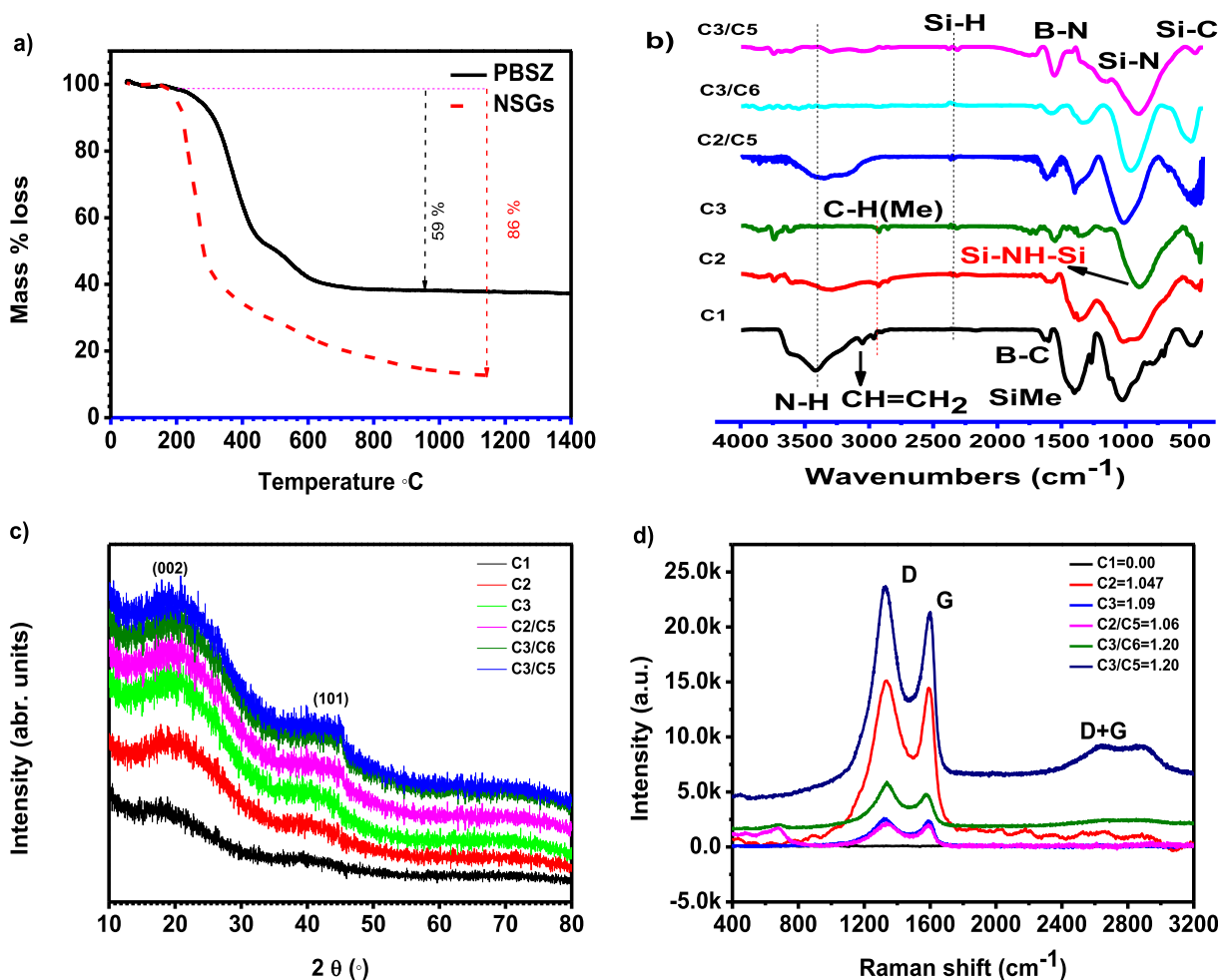
Fig. 2. (a) TGA thermogram of PBSZ and dual-doped NSGs at a heating rate of 10 K min^{-1} under Ar atmosphere, (b) FTIR analyses, (c) XRD patterns, confirming the ceramic nature and (d) Raman spectra of PDC SiBCN and nanocomposites anode active materials pyrolyzed at various temperatures.

Fig. 3d were associated with the C-O and C=O bonds due to the absorption of carbon dioxide on the specimen surface [48,49].

To investigate the electrochemical performance, the galvanostatic profiles (charge/discharge) of half-cell (composed of C3, C5 and C3/C5 nanocomposites as the anode and lithium foil as the reference and counter electrode) were tested. Fig. 4 shows the 1st,

21st, 41st, 121st and 251st cycles of galvanostatic curves at 450 mA g^{-1} for the respective anodes in the voltage range from 0.1 to 3.0 V. It shows that the C3/C5 nanocomposite anode has the highest initial discharge capacity of ~1612 mAh g^{-1} compared with the capacity of C3 (842.6 mAh g^{-1}) and C5 (1299.4 mAh g^{-1}) anode and a corresponding coulombic efficiency of 42%. However, after

Table 1
Elemental analyses of polyborosilazane and pyrolyzed anode specimens at different temperatures under argon atmosphere.

Specimens			Temperature	Composition (wt. %)[a]						Formula
Sample	Material	Ceramic Anodes		O	N	C	B	S	Si	
P	SiBCN	SiBCN	0	16.14	8.35	64.25	2.00	C	9.26	$Si_1B_{0.2}C_{6.9}N_{0.9}$
	NSGs	NSGs	0	25.57	15.57	51.15	C	7.72	c	–
P1[b]	SiBCN	C1	600 °C	16.80	6.55	59.61	1.28	C	15.79	$Si_1B_{0.08}C_{3.8}N_{0.4}$
	SiBCN	C2	800 °C	19.51	6.89	56.58	1.25	C	17.02	$Si_1B_{0.07}C_{3.3}N_{0.4}$
	SiBCN	C3	1000 °C	22.15	3.66	57.72	1.19	C	15.28	$Si_1B_{0.08}C_{3.8}N_{0.2}$
P2	NSGs	C4	600 °C	9.18	11.31	76.46	c	5.35	c	–
	NSGs	C5	800 °C	7.34	7.79	83.39	c	2.61	c	–
	NSGs	C6	1000 °C	8.61	4.08	86.75	c	0.98	c	–
P3	SiBCN/NSGs	C2/C5	800 °C	20.02	3.30	68.27	1.23	1.19	5.99	$Si_1B_{0.2}C_{11.4}N_{0.6}S_{0.2}$
	SiBCN/NSGs	C3/C6	1000 °C	20.73	2.11	69.55	1.17	0.38	6.06	$Si_1B_{0.2}C_{11.5}N_{0.3}S_{0.06}$
	SiBCN/NSGs	C3/C5	1000 °C/800 °C	17.12	4.39	72.47	1.11	0.45	5.46	$Si_1B_{0.2}C_{13.3}N_{0.8}S_{0.08}$

[a] Calculated from XPS spectrum refer to Fig. 3(a) and Fig. S3(b). Ceramic pyrolyzed at different temperature. The O$_2$ overview chiefly owing to the air fascination in ceramic material and O$_2$ persuaded during ceramic conversion.
[b] P1 polyborosilazane derived SiBCN.
[c] Not detected.
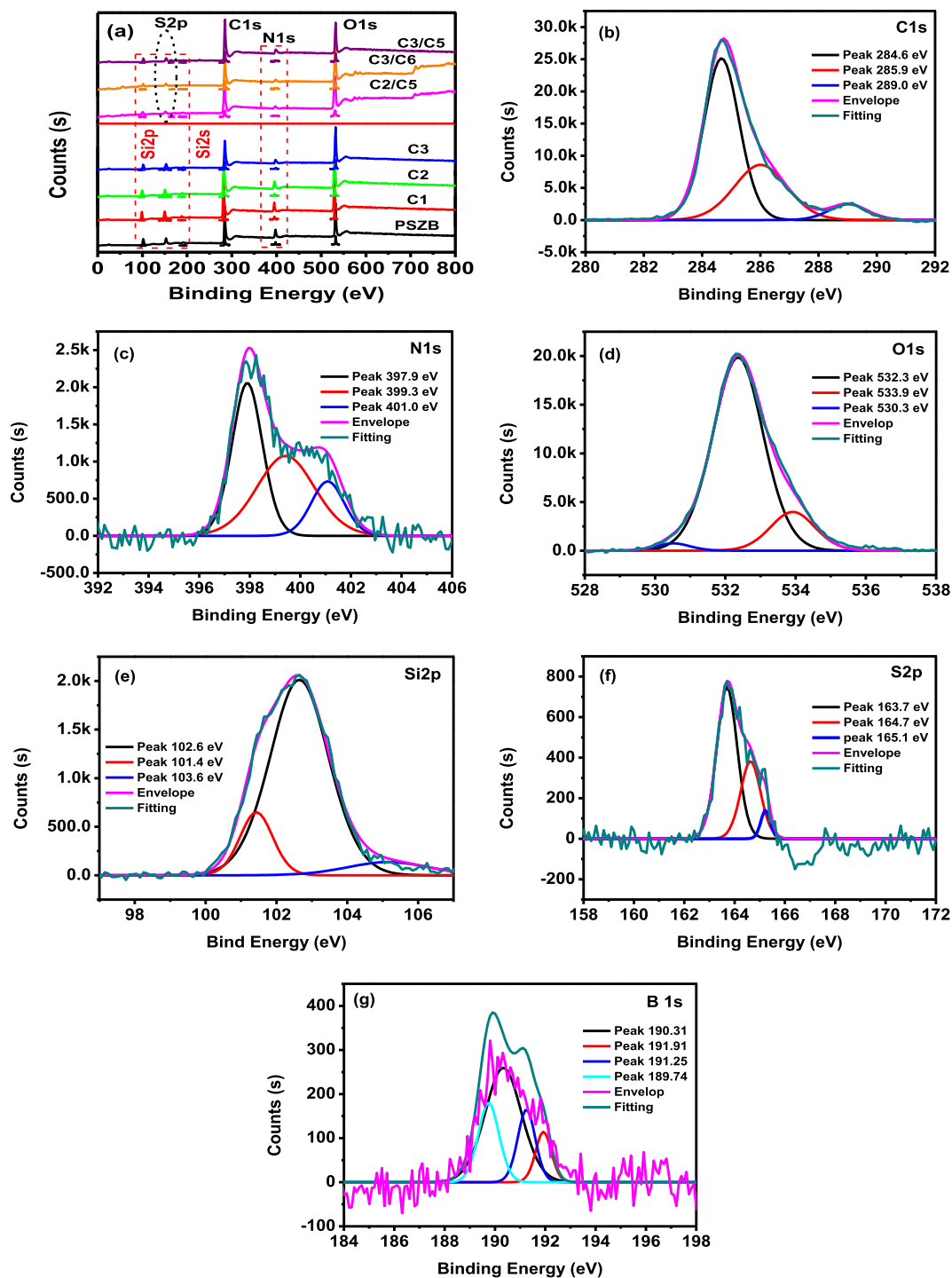
Fig. 3. XPS surface survey scan for polyborosilazane, its PDC and nanocomposites anode active material pyrolyzed at various temperatures (a); HRXPS spectrum of as-prepared C3/C5 nanocomposite anode material with shirely fitting deconvoluted C1s region (b), N1s region (c), O1s region (d), Si2p region (e), S2p region (f) and B1s region (g). The Si spectra in the survey scan originate from the underlying silicon substrate.

the first cycle, the coulombic efficiency dramatically increased to 99.7% at 251st cycle. Thus, the C3/C5 nanocomposite anode maintained a reversible capacity of ~731 mAh g^{-1} with 0.3% per cycle loss in the subsequent cycles. The discharge capacities of 1612.5, 655.9, 663.4, 718.7 and 733.5 mAh g^{-1} at a current density of 450, 650, 850, 1050 and 1250 mA g^{-1} for the C3/C5 nanocomposite anode were much higher than those of the C3 and C5 anodes at the corresponding cycles as shown in Table 2. However, at a narrow

potential range between 0.01 and 1.0 V, the C3/C5 nanocomposite anode delivered an initial coulombic efficiency of 77.93% with an irreversible capacity loss of 22.06% shown in Fig. S6. So, this performance (ICE) of C3/C5 nanocomposite anode in the narrow potential range was 35.34% greater than the ICE observed at high voltage range. This stable performance of C3/C5 nanocomposite with less cycle loss makes its suitability in commercial LIBs. The irreversible capacity loss during the initial cycles might be ascribed
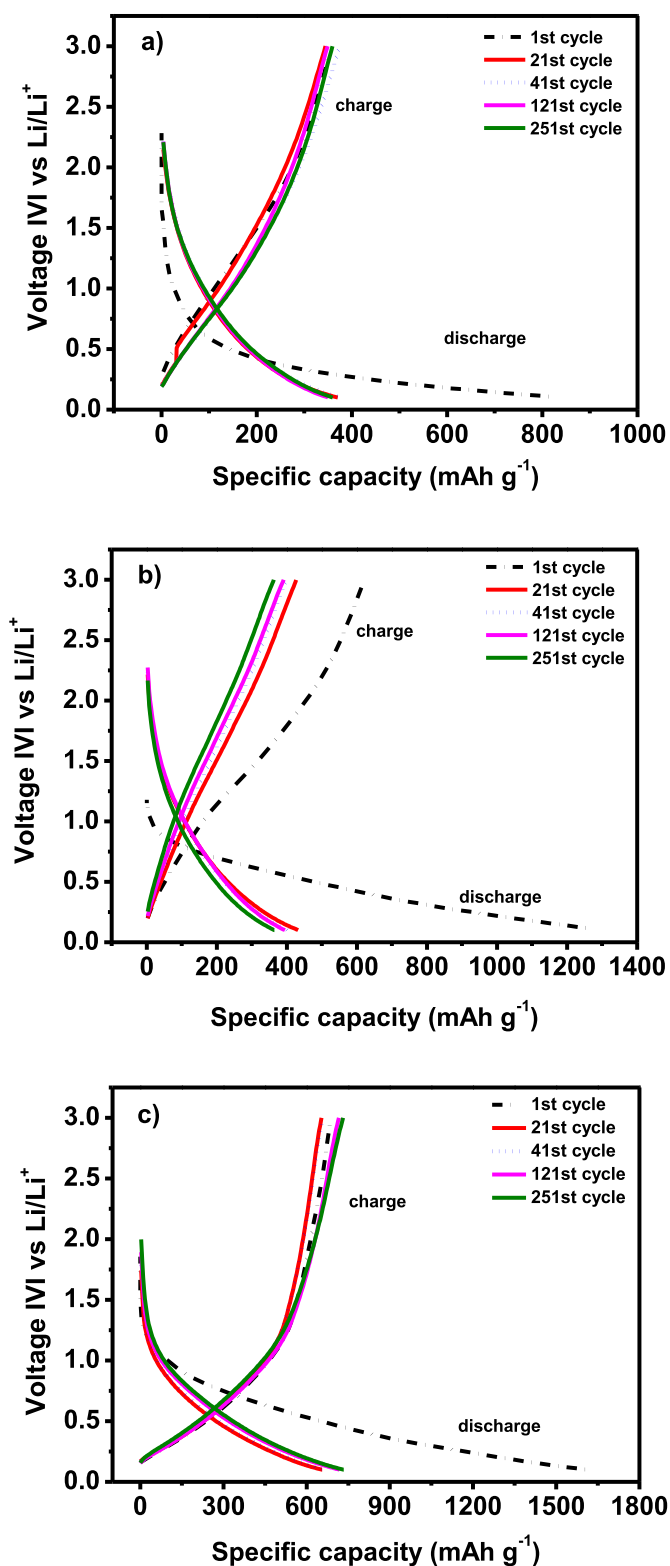
Fig. 4. Galvanostatic curves of the (a) C3 (b) C5 and (c) C3/C5 nanocomposite anodes at typical cycles.

to the formation of solid electrolyte interphases (SEIs) [50]. These side reactions occurred due to the chemical degradation, which was the main cause of lithium loss in LIBs. The Si/C @ 800 °C with different anode loading levels was examined to establish a better understanding of coulombic efficiency and specific capacity fade

rate. The half-cell anode with a higher anode level experienced a loss of 9.8% cycleable capacity upon the formation process of SEI. This capacity loss during the formation of SEI was attributed to the total surface area of anode material area exposed to the electrolyte. The half-cell anode with a higher level of loading (3.15 mg cm^{-2}) demonstrated a low average coulombic efficiency (~84.18%) on long cycling (20 cycles). The anode discharge limits met earlier due to the increasing amount of reduction reactions. With a higher level of loading (R = 3.15), the higher charge discharge rate of anode was ascribed to the larger surface area of the active anode composites. This hypothesis that the SEI is constantly dissolving and continuously reforming is based on the state of charge (SOC), as observed by paused galvanostatic cycling [51].

The increased capacities were correlated to the insertion of Li$^+$ into nanocomposites. This suggested that the insertion of NSGs into SiBCN played a key role in improving the Li-ion storage capacity. Moreover, to increase the stability of anode material, the cell was subjected to a short break at the charge potential of 3.0 V, while the discharge measurements started at 2.25 V. This slight shift in voltage potential of charge/discharge curves indicated fewer number of irreversible insertion sites of Li ions in the anode material [16].
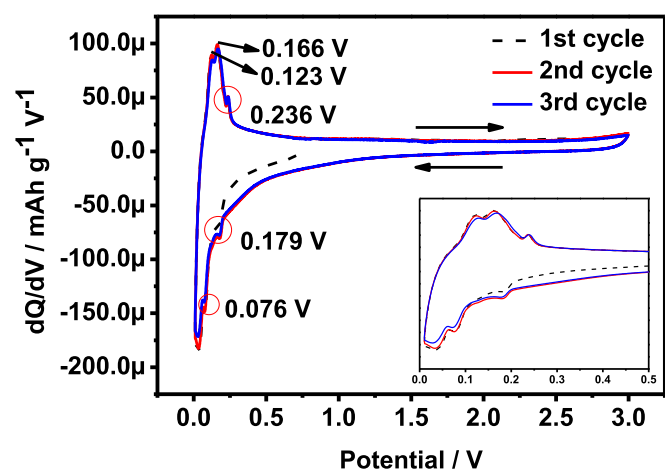
Fig. 5 presents the cyclic voltammograms of C3/C5 nanocomposite anode at an average scanning speed of 0.04 mVs^{-1}. Note that during the first anodic scan, the observed clear extensive oxidation peaks at 0.123, 0.166 and 0.236 V indicated the formation of SEI and the decomposition of the electrolyte on the surface of anode material. The slight reduction peaks (cathodic scan) were also observed at 0.076 and 0.179 V in the voltage range between 0.01 and 3.0 V. These results matched well with the galvanostatic profiles (Fig. 4).

Interestingly, there was obvious difference between the first scan and the subsequent cycles. However, all the cycles kept their potential constant. All the curves showed the voltage shift on the subsequent cycles, which was well consistent with the reported results [50,52,53]. This result confirmed the improved reversibility of the C3/C5 nanocomposite anode, and it was correlated to the dual-doped N/S on the lamellar layer of stacked graphene that were inserted into the SiBCN ceramic. During the subsequent cycles, the undetectable decrease in the peak intensity further confirmed the reversible electrochemical reactions of C3/C5 nanocomposite. In fact, N and S dual-doped graphene was able to generate more extrinsic defects and active sites and simultaneously increased the conductivity and the electrochemical activity. Moreover, it absorbed the Li$^+$ ions on various active sites and promoted rapid charge-transfer reaction, while the larger interlayer spacing facilitated the intercalation/extraction of Li$^+$ ions into the graphitic shells.

In addition, the C3/C5 nanocomposite anode demonstrated an improved rate performance than the C3 and C5 anode used in the lithium ion batteries. In Fig. 6a, the C3/C5 nanocomposite anode showed a relatively superior rate capability with an average capacity of ~785 mAh g^{-1} at a current density of 450 mA g^{-1} between 0.1 and 3.0 V, it dropped with increasing the current density, i.e., 477, 220, 142, and 99 mAh g^{-1} at a corresponding current density of 650, 850, 1050 and 1250 mA g^{-1}. The charge capacity of ~774 mAh g^{-1} was stabilized at the same current density. A similar decreasing trend of charge capacity was also observed for the as-prepared C3 anode with increasing the current density from 450 to 1250 mA g^{-1}. The C3 anode exhibited the charge capacities of 327, 253, 152, 110, and 71 mAh g^{-1} at a corresponding current density of 200, 400, 600, 800, 1000 mA g^{-1}. When the current density was increased from 450 to 1250 mA g^{-1}, the discharge capacity similarly returned back to ~327 mAh g^{-1} for C3 anode. However the as-prepared C5 anode exhibited an initial discharge capacity of ~397 mAh g^{-1} at a current density of 200 mA g^{-1}. The capacity decreased to ~267 mAh

Table 2
The galvanostatic charge (C_{charge}) and discharge ($C_{discharge}$) data of C3/C5 nanocomposite anode compared to C3 and C5 anode. The error in the data calculation is $\pm 0.1\%$.

Anodes specimen	Cycles No. (nth)	C_{rev} (mAh g^{-1})	C_{ch} (mAh g^{-1})	C_{irrev} (mAh g^{-1})	Cycle loss (%)	Coulombic efficiency (η, %)
C3	1st	842.6	357.3	485.3	57.6	42.4
	21st	370.1	344.7	25.4	6.9	93.1
	41st	377.3	374.8	2.5	0.7	99.3
	121st	350.1	348.9	1.2	0.3	99.7
	251st	359.8	359.2	0.6	0.2	99.8
C5	1st	1299.4	620.9	678.5	52.2	47.78
	21st	432.3	426.8	5.5	1.27	98.73
	41st	402.0	399.0	3.0	0.75	99.25
	121st	394.4	390.9	3.5	0.887	99.11
	251st	364.3	362.7	1.6	0.439	99.56
C3/C5	1st	1612.5	687.3	925.2	57.4	42.6
	21st	655.9	653.1	2.8	0.4	99.6
	41st	663.4	658.7	4.7	0.7	99.3
	121st	718.7	716.1	2.6	0.3	99.6
	251st	733.5	731.5	2.0	0.3	99.7

Fig. 5. (a) CV curves of C3/C5 nanocomposite anodes at an average scanning rate of 0.04 mV s $^{-1}$.

g^{-1} when the current density increased to 100 mA g^{-1}. The capacity returned to ~389 mAh g^{-1} when the current density returned again to 200 mA g^{-1}. This stable performance with 99% coulombic efficiency was attributed to the doped N/S on the lamellar layer of the stacked graphene [54]. These results advocated that the insertion of NSGs into SiBCN matrix was suitable for serving as anode for LIBs.

To further confirm the cycle stability of freshly assembled anodes, prolonged symmetric cycling was subjected at a current density of 450 mA g^{-1} for the C1-C3, C2/C5-C3/C5 nanocomposite anodes and 200 mA g^{-1} for the C4-C6 anodes. Fig. 6b shows the specific capacity of the as-prepared C1-C3 anodes. The C3 anode reached a capacity of ~365 mAh g^{-1} after 500 cycles, indicating the remarkably improved performance for the LIBs compared to the C1 and C2 anodes pyrolyzed at 600 and 800 °C, whose specific capacity retained stable but with a lower charge capacity of ~77 and ~112 mAh g^{-1}. This better structural integrity of C3 anode at 450 mA g^{-1} was confirmed by the HRTEM and SEM, as shown in Fig. S2(a and b) and 7. In addition, the as-prepared C5 anode displayed a high charge capacity of ~393 mAh g^{-1} at a current density of 200 mA g^{-1} compared to the as-prepared C4 and C6 anode pyrolyzed at 600 and 1000 °C (Fig. 6c), whose specific capacity was ~205 and ~350 mAh g^{-1}. This high charge capacity compared to SiBCN anodes was attributed to the larger surface area from the NSGs, which provided appropriate contact of space for the rapid diffusion of lithium-ions within the electrode material, while the wide interlayer space enabled the high Li-intercalation of kinetics

[55]. Moreover, the 2D structure of NSGs ensured the Li-ion storage [56] and shortened the length of Li-ion diffusion.

Further, the nanocomposite anodes @ various temperatures shown in Fig. 6d, e were evaluated for their electrochemical performances. The C3/C5 nanocomposite anode delivered an improved capacity of ~785 mAh g^{-1} in the voltage window of 0.1–3.0 V at 450 mA g^{-1} in comparison with C2/C5 (~390 mAh g^{-1}) and C3/C6 (~430 mAh g^{-1}) nanocomposite anodes at low level loading shown in Fig. 6e. At high level loading and density of 3.15 mg cm^{-2} and 2.787 mg cm^{-3}, the cycle loss of C3/C5 nanocomposite anode was 9.8% less than at low level loading. (Fig. S5 in the supporting information). It can be observed that the stability was maintained with a capacity retention of 99% even for long term cycling. In addition, the stable performance at high voltage further suggested its suitability for practical applications. This high performance was comparable to previously reported studies on graphene shown in Table 3. This improved reversible capacity with almost 99% of coulombic efficiency after 800 cycles was caused by the insertion of NSGs into SiBCN ceramic. The resulted nanocomposites showed a better electrical contact between the copper foil and the SiBCN particles and stable structural stability inserted provided by NSGs. The enhanced electrochemical performance was due to the increased extrinsic defects and active sites. Thus, the structural distortion towards stacked graphene increased the conductivity and active sites for Li-ion insertion [22,30].

After electrochemical cycling, the recycled cells were dissembled for the post-morphological analysis. The SEM (Fig. 7b, c and 8b, d) was performed for the C3 and C3/C5 nanocomposite anode materials and their surface morphologies were examined. The pre-cycled C3 anode material mainly showed interconnected ceramic particles and furry carbon black (Fig. 7a). While the C3/C5 nanocomposite anode material exhibited similar morphologies to typical lamellar layers of the NSGs in the SiBCN matrix. This reveals that NSGs in nanocomposite acted as supporting material for SiBCN ceramic as shown in Fig. 8 (a, c). The C3 anode material had smaller particles due to the electrostatic repulsion of oxygen containing groups on the surface of C5 anode material. In addition, the particles for the C3/C5 nanocomposite anode materials were more uniform than those of the C3 anode material. However, SiBCN ceramic showed an asymmetrical enormous chunk form with small particles on the surface. Fig. 8a, c shows the existence of NSGs ceramic on the surface of nanocomposites. The EDS analysis of the captured region in Fig. 7d-h showed the presence of C, Si, N and B in the C3 anode material. Remarkably, the post cycled anodes were mainly intact without clear signs of cracking and pulverization as shown in Fig. 8 (b, d). The absence of cracks on the surface of anode suggested a stable cycling performance [57]. The cycled C3/C5
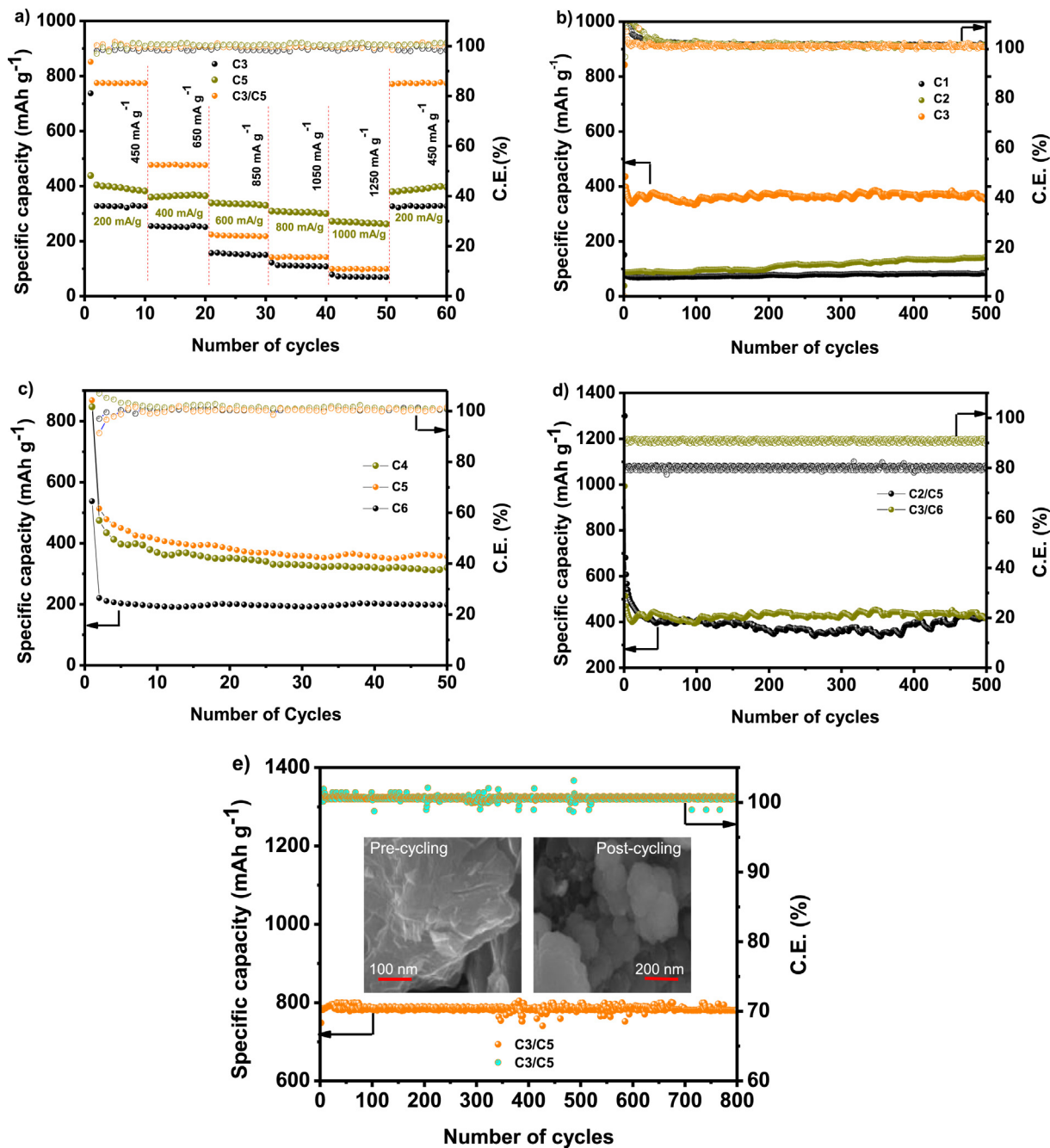
Fig. 6. (a) Rate capabilities Li-storage performance of the C3,C5 and C3/C5 nanocomposite anodes (a), Cycling performance and coulombic efficiency of the as-prepared C1-C3 anodes at 450 mA g^{-1} (b) and C4-C6 anodes at 200 mA g^{-1} (c). The prolong cycling behaviour and coulombic efficiency of the C3/C5 nanocomposite anode at 450 mA g^{-1} (e). A comparison of capacity potential of as-prepared nanocomposite anodes can be seen in (d). The inset shows the SEM micrographs of pre-and post-cycled C3/C5 nanocomposite anode material.

Table 3
Summary for the performance of SiBCN/NSGs nanocomposite and PDC based anode materials reported previously.

Anode material	Current density (mA g^{-1})	Capacity (mA h g^{-1})	nth cycle	Coulombic efficiency (η, %)	References
Sulfur/nitrogen dual-doped porous graphene	50	440	100	56.41	[58]
Nitrogen-doped graphene nanosheets	100	452	100	99.0	[59]
Nitrogen-doped graphene	100	600	50	63.20	[60]
Graphene/N-doped carbon	100	669	200	60.88	[61]
Nitrogen-self-doped graphene	50	682	95	57.94	[62]
Porous graphene films	50	715	50	67.32	[63]
Nitrogen and fluorine co-doped graphene	100	765	50	71.29	[64]
SiBCN/NSGs	450	785	800	99.0	This work
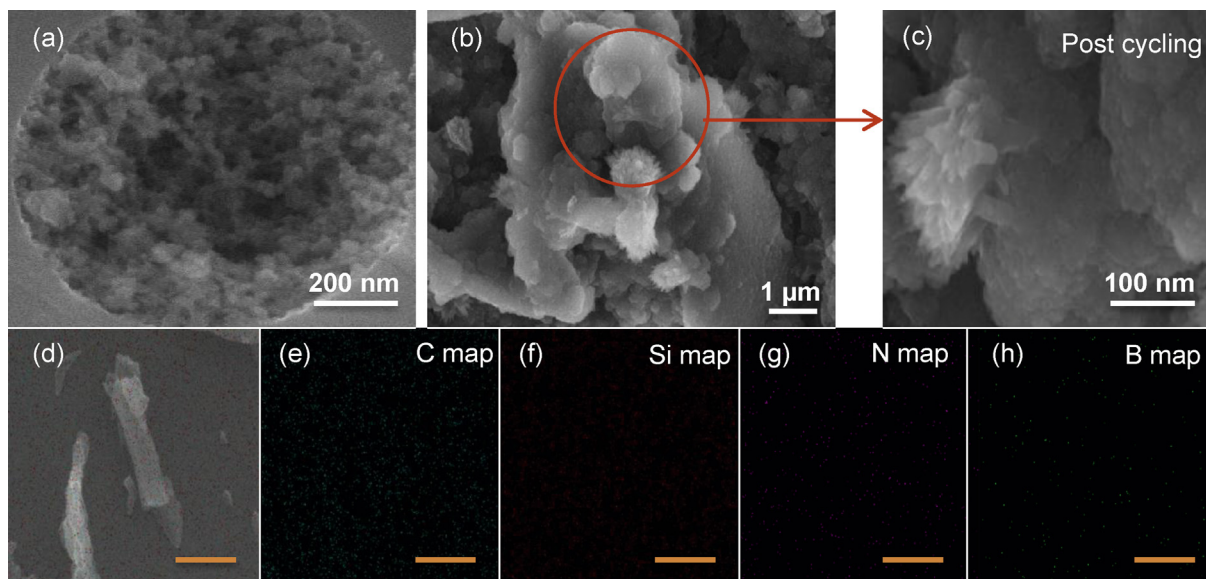
Fig. 7. Comparison of SEM images of the as-prepared C3 anode material (a) with the post-cycled anode material (dissembled in charging state) (b). Higher-magnification SEM image of post-cycled C3 anode material (c), EDS captured region of C3 anode material (d), showed the elemental mapping images (d, e, f and g) of the corresponding as-prepared C3 anode material. Mapping scale bar is 500 nm.
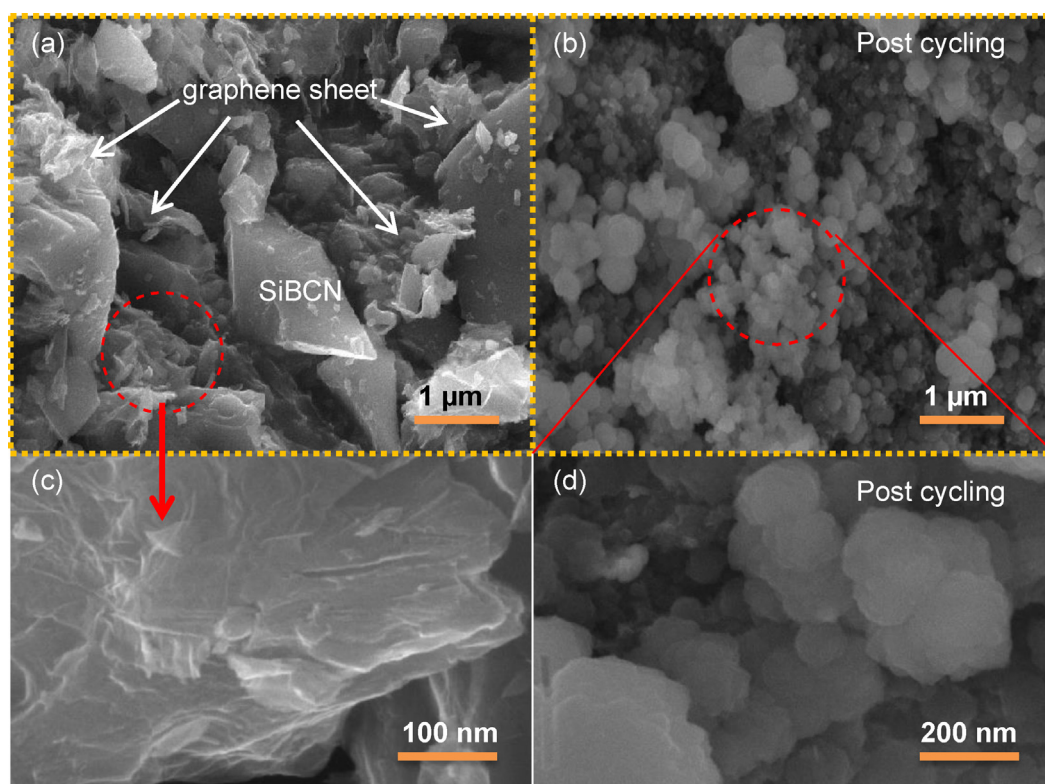
Fig. 8. SEM micrograph of C3/C5 nanocomposite anode material (a, c) before electrochemical cycles showed stacked layer on the surface, and (b,d) post-cycled anode after prolonged 800 cycles, nanocomposite showed stretching and rearrangement of SiBCN/NSGs before cycling and negligible stretching arrangement occurred after cycling.

nanocomposite anode showed amorphous and uniform structure with uneven layers of stacked graphene, which was corroborated to a significantly improved cycling performance as shown earlier.

4. Conclusion

The effects of nitrogen sulfur dual-doped graphene (NSG) sheets on the electrochemical performance of silicon boron carbon nitride (SiBCN) ceramics were studied to serve as an anode material in lithium ion batteries. The active anode material was obtained via pyrolysis at 600, 800 and 1000 °C. Thus, the pyrolysis played a key role in the cycling competence of nanocomposite anodes. The as-prepared C3/C5 nanocomposite anode gave a specific capacity of ~785 mAh g^{-1} at 450 mA g^{-1} after 800 cycles with a stable capacity retention of 99%, which was higher than the specific capacity of C3 and C5 anode. This improved performance was attributed to the stacked graphene structure and heteroatom doping. The outstanding performance of the C3/C5 nanocomposite anode was mainly due to the conducting ceramic nanocomposite with stacked layers, which acted as a supporting material with stable structure that facilitated the Li-ion insertion. In addition, the stacked layer network structure further prevented the delamination caused by the Li-ions insertion and extraction during cycling. The incorporation of NSGs into SiBCN ceramic revealed a novel strategy of developing the anode material, which influenced the performance of SiBCN anode in LIBs. Compared with metals and ceramics [65–69], these unique silicon-based carbon materials have great potential to be used for other applications including electromagnetic interference shielding [70–75], energy application such as fuel cells and solar cells [76–81], adsorbents for heavy metal removal and others [82–88], and serving as fillers for structural and functional nanocomposites [89–100].

Acknowledgements

Appendix A. Supplementary data

Supplementary data to this article can be found online at https://doi.org/10.1016/j.electacta.2018.11.088.

References

[1] J.L. Gomez-Ballesteros, P.B. Balbuena, Reduction of electrolyte components on a coated Si anode of lithium-ion batteries, J. Phys. Chem. Lett. 8 (2017) 3404–3408.

[2] D. Sui, Y. Xie, W. Zhao, H. Zhang, Y. Zhou, X. Qin, Y. Chen, A high-performance ternary Si composite anode material with crystal graphite core and amorphous carbon shell, J. Power Sources 384 (2018) 328–333.

[3] T.D. Hatchard, J.R. Dahn, In situ XRD and electrochemical study of the reaction of lithium with amorphous silicon, J. Electrochem. Soc. 151 (2004) A838–A842.

[4] T. Moon, C. Kim, B. Park, Electrochemical performance of amorphous-silicon thin films for lithium rechargeable batteries, J. Power Sources 155 (2006) 391–394.

[5] S. Basu, S. Suresh, K. Ghatak, S.F. Bartolucci, T. Gupta, P. Hundekar, N. Koratkar, Utilizing van der Waals slippery interfaces to enhance the electrochemical stability of Silicon film anodes in Lithium-ion batteries, ACS

[6] P.L.S.G. Poizot, S. Laruelle, S. Grugeon, L. Dupont, J.M. Tarascon, Nano-sized transition-metal oxides as negative-electrode materials for lithium-ion batteries, Nature 407 (2000) 496–499.

[7] J.M. Tarascon, M. Armand, Issues and challenges facing rechargeable lithium batteries, in: Materials for Sustainable Energy: a Collection of Peer-reviewed Research and Review Articles from Nature Publishing Group, 2001, pp. 171–179.

[8] D. Ahn, R. Raj, Cyclic stability and C-rate performance of amorphous silicon and carbon based anodes for electrochemical storage of lithium, J. Power Sources 196 (2001) 2179–2186.

[9] D. Ahn, R. Raj, Thermodynamic measurements pertaining to the hysteretic intercalation of lithium in polymer-derived silicon oxycarbide, J. Power Sources 195 (2010) 3900–3906.

[10] Y. Feng, Electrochemical properties of heat-treated polymer-derived SiCN anode for lithium ion batteries, Electrochim. Acta 55 (2010) 5860–5866.

[11] H. Fukui, N. Nakata, K. Dokko, B. Takemura, H. Ohsuka, T.K. Kanamura, Lithiation and delithiation of silicon oxycarbide single particles with a unique microstructure, ACS Appl. Mater. Interfaces 3 (2011) 2318–2322.

[12] H. Fukui, H. Ohsuka, T. Hino, K. Kanamura, Polysilane/acenaphthylene blends toward Si–O–C composite anodes for rechargeable lithium-ion batteries, J. Electrochem. Soc. 158 (2011) 158. A550–A555.

[13] M. Graczyk-Zajac, G. Mera, J. Kaspar, R. Riedel, Electrochemical studies of carbon-rich polymer-derived SiCN ceramics as anode materials for lithium-ion batteries, J. Eur. Ceram. Soc. 30 (2010) 3235–3243.

[14] X. Lou, C. Lin, Q. Luo, J. Zhao, B. Wang, J. Li, Q. Shao, X. Guo, N. Wang, Z. Guo, Crystal structure modification enhanced FeNb11O29 anodes for lithium-ion batteries, ChemElectroChem 4 (2017) 3171–3180.

[15] C. Lin, H. Hu, C. Cheng, K. Sun, X. Guo, Q. Shao, J. Li, N. Wang, Z. Guo, Nano-TiNb2O7/carbon nanotubes composite anode for enhanced lithium-ion storage, Electrochim. Acta 260 (2018) 65–72.

[16] D. Su, Y. Li, Y. Feng, J. Jin, Electrochemical properties of polymer-derived SiCN materials as the anode in lithium ion batteries, J. Am. Ceram. Soc. 92 (2009) 2962–2968.

[17] L. Yan, H. Wang, D. Huang, H. Luo, Electrodes with high conductivities for high performance lithium/sodium ion batteries, Eng. Sci. 1 (2018) 4–20. www.doi.org/10.30919/es.180318.

[18] T. Bhardwaj, A. Antic, B. Pavan, V. Barone, B.D. Fahlman, Enhanced electrochemical lithium storage by graphene nanoribbons, J. Am. Chem. Soc. 132 (2010) 12556–12558.

[19] A.L.M. Reddy, A. Srivastava, S.R. Gowda, H. Gullapalli, M. Dubey, P.M. Ajayan, Synthesis of nitrogen-doped graphene films for lithium battery application, ACS Nano 4 (2010) 337–6342.

[20] Z.S. Wu, W. Ren, L. Xu, F. Li, H.M. Cheng, Doped graphene sheets as anode materials with superhigh rate and large capacity for lithium ion batteries, ACS Nano 5 (2011) 5463–5471.

[21] W. Ai, L. Xie, Z. Du, Z. Zeng, J. Liu, H. Zhang, Y. Huang, W. Huang, T. Yu, A novel graphene-polysulfide anode material for high-performance lithium-ion batteries, Sci. Rep. 3 (2013) 2341.

[22] C. Zhang, N. Mahmood, H. Yin, F. Liu, Y. Hou, Synthesis of phosphorus-doped graphene and its multifunctional applications for oxygen reduction reaction and lithium ion batteries, Adv. Mater. 25 (2013) 4932–4937.

[23] W. Deng, T. Kang, H. Liu, J. Zhang, N. Wang, N. Lu, Y. Ma, A. Umar, Z. Guo, Potassium hydroxide activated and nitrogen doped graphene with enhanced supercapacitive behavior, Sci. Adv. Mater. 10 (2018) 937–949.

[24] P. Bhunia, E. Hwang, Y. Yoon, E. Lee, S. Seo, H. Lee, Synthesis of highly n-type graphene by using an ionic liquid, Chem. Eur. J. 18 (2012) 12207–12212.

[25] a) Z. Jin, J. Yao, C. Kittrell, J.M. Tour, Large-scale growth and characterizations of nitrogen-doped monolayer graphene sheets, ACS Nano 5 (2011) 4112–4117.

[26] B. Guo, X.G. Sun, G.M. Veith, Z. Bi, S.M. Mahurin, C. Liao, C. Bridges, M.P. Paranthaman, S. Dai, Nitrogen-enriched carbons from alkali salts with high coulombic efficiency for energy storage applications, Adv. Energy Mater. 3 (2013) 708–712.

[27] D. Li, L. Zhang, H. Chen, J. Wang, L.X. Ding, S. Wang, P.J. Ashman, H. Wang, Graphene-based nitrogen-doped carbon sandwich nanosheets: a new capacitive process controlled anode material for high-performance sodium-ion batteries, J. Mater. Chem. A 4 (2016) 8630–8635.

[28] H. Liu, M. Jia, B. Cao, R. Chen, X. Lv, R. Tang, F. Wu, B. Xu, Nitrogen-doped carbon/graphene hybrid anode material for sodium-ion batteries with excellent rate capability, J. Power Sources 319 (2016) 195–201.

[29] H.G. Wang, Z. Wu, F.L. Meng, D.L. Ma, X.L. Huang, Thin space (1/6-em). FL Meng [thin space (1/6-em)], DL Ma [thin space (1/6-em)], XL Huang [thin space (1/6-em)], LM Wang and XB Zhang, ChemSusChem 6 (2013) 56–60.

[30] J.P. Paraknowitsch, A. Thomas, Doping carbons beyond nitrogen: an overview of advanced heteroatom doped carbons with boron, sulphur and phosphorus for energy applications, Energy Environ. Sci. 6 (2013) 2839–2855.

[31] H. Wang, C. Zhang, Z. Liu, L. Wang, P. Han, H. Xu, K. Zhang, S. Dong, L. Yao, G. Cui, Nitrogen-doped graphene nanosheets with excellent lithium storage properties, J. Mater. Chem. 21 (2011) 5430–5434.

[32] X. Liu, J. Zhang, S. Guo, N. Pinna, Graphene/N-doped carbon sandwiched nanosheets with ultrahigh nitrogen doping for boosting lithium-ion batteries, J. Mater. Chem. A 4 (2016) 1423–1431.

[33] D.C. Marcano, D.V. Kosynkin, J.M. Berlin, A. Sinitskii, Z. Sun, A. Slesarev,

L.B. Alemany, W. Lu, J.M. Tour, Improved synthesis of graphene oxide, ACS Nano 4 (2010) 4806–4814.

[34] B. Kirubasankar, V. Murugadoss, J. Lin, T. Ding, M. Dong, H. Liu, J. Zhang, T. Li, N. Wang, Z. Guo, S. Angaiaha, In-situ grown nickel selenide onto graphene nanohybrid electrodes for high energy density asymmetric supercapacitors, Nanoscale 10 (2018) 20414–20425.

[35] J. Gu, C. Liang, J. Dang, W. Dong, Q. Zhang, Ideal dielectric thermally conductive bismaleimide nanocomposites filled with polyhedral oligomeric silsesquioxane functionalized nanosized boron nitride, RSC Adv. 6 (2016) 35809–35814.

[36] S. Choi, D.S. Jung, J.W. Choi, Scalable fracture-free SiOC glass coating for robust silicon nanoparticle anodes in lithium secondary batteries, Nano Lett. 14 (2014) 7120–7125.

[37] R.J. Corriu, N. Devylder, C. Guérin, B. Henner, A. Jean, Oligomers with silicon, germanium and transit ion metal groups: synthesis and characterization of metal-containing poly [(silylene) diacetylenes] and poly [(germylene) diacetylenes], Organometallics 13 (1994) 3194–3202.

[38] N.S. Choong Kwet Yive, R.J.P. Corriu, D. Leclercq, P.H. Mutin, A. Vioux, Silicon carbonitride from polymeric precursors: thermal cross-linking and pyrolysis of oligosilazane model compounds, Chem. Mater. 4 (1992) 141–146.

[39] J. Schuhmacher, F. Berger, M. Weinmann, J. Bill, F. Aldinger, K. Müller, Solid-state NMR and FT IR studies of the preparation of Si–B–C–N ceramics from boron-modified polysilazanes, Appl. Organomet. Chem. 15 (2001) 809–819.

[40] N. Janakiraman, M. Weinmann, J. Schuhmacher, K. Muller, J. Bill, F. Aldinger, P. Singh, Thermal stability, phase evolution, and crystallization in Si-B-C-N ceramics derived from a polyborosilazane precursor, J. Am. Ceram. Soc. 85 (2002) 1807–1814.

[41] M. Idrees, S. Batool, Q. Hussain, H. Ullah, M.I. Al-Wabel, M. Ahmad, J. Kong, High-efficiency remediation of cadmium (Cd^{2+}) from aqueous solution using poultry manure—and farmyard manure—derived biochars, Separ. Sci. Technol. 51 (2016) 2307–2317.

[42] J. Schuhmacher, F. Berger, M. Weinmann, J. Bill, F. Aldinger, K. Müller, Solid-state NMR and FT IR studies of the preparation of Si–B–C–N ceramics from boron-modified polysilazanes, Appl. Organomet. Chem. 15 (2001) 809–819.

[43] G. Lian, X. Zhang, M. Tan, S. Zhang, D. Cui, Q. Wang, Facile synthesis of 3D boron nitride nanoflowers composed of vertically aligned nanoflakes and fabrication of graphene-like BN by exfoliation, J. Mater. Chem. 21 (2011) 9201–9207.

[44] S. Bernard, M. Weinmann, P. Gerstel, P. Miele, F. Aldinger, Boron-modified polysilazane as a novel single-source precursor for SiBCN ceramic fibers: synthesis, melt-spinning, curing and ceramic conversion, J. Mater. Chem. 15 (2005) 289–299.

[45] C. Luo, T. Jiao, Y. Tang, J. Kong, Excellent electromagnetic wave absorption of iron-containing SiBCN ceramics at 1158 K high-temperature, Adv. Eng. Mater. 20 (2018) 1701168.

[46] C. Luo, Y. Tang, T. Jiao, J. Kong, High-temperature stable and metal-free electromagnetic wave-absorbing SiBCN ceramics derived from carbon-rich hyperbranched polyborosilazanes, ACS Appl. Mater. Interfaces 10 (2018) 28051–28061.

[47] J. Kong, M. Wang, J. Zou, L. An, Soluble and meltable hyperbranched polyborosilazanes toward high-temperature stable SiBCN ceramics, ACS Appl. Mater. Interfaces 7 (2015) 6733–6744.

[48] W. Zhao, Y. Tang, J. Xi, J. Kong, Functionalized graphene sheets with poly (ionic liquid) s and high adsorption capacity of anionic dyes, Appl. Surf. Sci. 326 (2015) 276–284.

[49] C. Luo, W. Duan, X. Yin, J. Kong, Microwave-absorbing polymer-derived ceramics from cobalt-coordinated poly (dimethylsilylene) diacetylenes, J. Phys. Chem. C 120 (2016) 18721–18732, 120.

[50] Q. Wang, L. Jiao, Y. Han, H. Du, W. Peng, Q. Huan, D. Song, Y. Si, Y. Wang, H. Yuan, CoS2 hollow spheres: fabrication and their application in lithium-ion batteries, J. Phys. Chem. C 115 (2011) 8300–8304.

[51] V. Nilsson, R. Younesi, D. Brandell, K. Edström, P. Johansson, Critical evaluation of the stability of highly concentrated LiTFSI-Acetonitrile electrolytes vs. graphite, lithium metal and LiFePO 4 electrodes, J. Power Sources 384 (2018) 334–341.

[52] Y. Wang, J. Wu, Y. Tang, X. Lü, C. Yang, M. Qin, F. Huang, X. Li, X. Zhang, Phase-controlled synthesis of cobalt sulfides for lithium ion batteries, ACS Appl. Mater. Interfaces 4 (2012) 4246–4250.

[53] J. Xie, S. Liu, G. Cao, T. Zhu, X. Zhao, Self-assembly of CoS2/graphene nano-architecture by a facile one-pot route and its improved electrochemical Li-storage properties, Nano Energy 2 (2013) 49–56.

[54] Z. Luo, J. Zhou, X. Cao, S. Liu, Y. Cai, L. Wang, A. Pan, S. Liang, Graphene oxide templated nitrogen-doped carbon nanosheets with superior rate capability for sodium ion batteries, Carbon 122 (2017) 82–91.

[55] Y. Matsuo, J. Taninaka, K. Hashiguchi, T. Sasaki, Q. Cheng, Y. Okamoto, N. Tamura, Effect of oxygen contents in graphene like graphite anodes on their capacity for lithium ion battery, J. Power Sources 396 (2018) 134–140.

[56] R. Ruffo, S.S. Hong, C.K. Chan, R.A. Huggins, Y. Cui, Impedance analysis of silicon nanowire lithium ion battery anodes, J. Phys. Chem. C 113 (2009) 11390–11398.

[57] H. Shan, X. Li, Y. Cui, D. Xiong, B. Yan, D. Li, A. Lushington, X. Sun, Sulfur/nitrogen dual-doped porous graphene aerogels enhancing anode performance of lithium ion batteries, Electrochim. Acta 205 (2016) 188–197.

[58] X. Li, D. Geng, Y. Zhang, X. Meng, R. Li, X. Sun, Superior cycle stability of nitrogen-doped graphene nanosheets as anodes for lithium ion batteries,

[59] Electrochem. Commun. 13 (2011) 822–825.

[59] Z. Xing, Z. Ju, Y. Zhao, J. Wan, Y. Zhu, Y. Qiang, Y. Qian, One-pot hydrothermal synthesis of Nitrogen-doped graphene as high-performance anode materials for lithium ion batteries, Sci. Rep. 6 (2016) 26146.

[60] X. Liu, J. Zhang, S. Guo, N. Pinna, Graphene/N-doped carbon sandwiched nanosheets with ultrahigh nitrogen doping for boosting lithium-ion batteries, J. Mater. Chem. A 4 (2016) 1423–1431.

[61] C. He, R. Wang, H. Fu, P.K. Shen, Nitrogen-self-doped graphene as a high capacity anode material for lithium-ion batteries, J. Mater. Chem. A 1 (2013) 14586–14591.

[62] X. Zhang, J. Zhou, C. Liu, X. Chen, H. Song, A universal strategy to prepare porous graphene films: binder-free anodes for high-rate lithium-ion and sodium-ion batteries, J. Mater. Chem. A 4 (2016) 8837–8843.

[63] S. Huang, Y. Li, Y. Feng, H. An, P. Long, C. Qin, W. Feng, Nitrogen and fluorine co-doped graphene as a high-performance anode material for lithium-ion batteries, J. Mater. Chem. A 3 (2015) 23095–23105.

[64] S. Huang, L. Zhang, J. Zhu, S.P. Jiang, P.K. Shen, Crumpled nitrogen-and boron-dual-self-doped graphene sheets as an extraordinary active anode material for lithium ion batteries, J. Mater. Chem. A 4 (2016) 14155–14162.

[65] Z.Y. Zhao, R.G. Guan, J.H. Zhang, Z.Y. Zhao, P.K. Bai, Effects of process parameters of semisolid stirring on microstructure of Mg-3Sn-1Mn-3SiC (wt%) strip processed by rheo-rolling, Acta Metall. Sin. (Engl. Lett.) 30 (2017) 66–72.

[66] Z. Zhao, P. Bai1, R. Guan, V. Murugadoss, H. Liu, X. Wang, Z. Guo, Microstructural evolution and mechanical strengthening mechanism of Mg-3Sn-1Mn-1La alloy after heat treatments, Mater. Sci. Eng. A 734 (2018) 200–209.

[67] H. Kang, Z. Cheng, H. Lai, H. Ma, Y. Liu, X. Mai, Y. Wang, Q. Shao, L. Xiang, X. Guo, Z. Guo, Superlyophobic anti-corrosive and self-cleaning titania robust mesh membrane with enhanced oil/water separation, Separ. Purif. Technol. 201 (2018) 193–204.

[68] Y. Guo, Y. Li, X. Lou, J. Guan, Y. Li, X. Mai, H. Liu, C.X. Zhao, N. Wang, C. Yan, G. Gao, Improved extraction of cobalt and lithium by reductive acid from spent lithium-ion batteries via mechanical activation process, J. Mater. Sci. 53 (2018) 13790–13800.

[69] C. Wang, B. Mo, Z. He, Q. Shao, D. Pan, E. Wujick, J. Guo, X. Xie, X. Xie, Z. Guo, Crosslinked norbornene copolymer anion exchange membrane for fuel cells, J. Membr. Sci. 556 (2018) 118–125.

[70] N. Wu, C. Liu, D. Xu, J. Liu, W. Liu, Q. Shao, Z. Guo, Enhanced electromagnetic wave absorption of three-dimensional porous Fe3O4/C composite flowers, ACS Sustain. Chem. Eng. 6 (2018) 12471–12480.

[71] Z. Wang, R. Wei, J. Gu, H. Liu, C. Liu, C. Luo, J. Kong, Q. Shao, N. Wang, Z. Guo, X. Liu, et al., Ultralight, highly compressible and fire-retardant graphene aerogel with self-adjustable electromagnetic wave absorption, Carbon 139 (2018) 1126–1135.

[72] K. Zhang, G.H. Li, L.M. Feng, N. Wang, J. Guo, K. Sun, K.X. Yu, J.B. Zeng, T. Li, Z. Guo, M. Wang, Ultralow percolation threshold and enhanced electromagnetic interference shielding in poly(L-lactide)/multi-walled carbon nanotubes nanocomposites with electrically conductive segregated networks, J. Mater. Chem. C 5 (2017) 9359–9369.

[73] Z. Guo, P. Xie, F. Dang, B. He, J. Lin, R. Fan, C. Hou, H. Liu, J.X. Zhang, Y. Ma, et al., Bio-gel derived nickel/carbon nanocomposites with enhanced microwave absorption, J. Mater. Chem. C 6 (2018) 8812–8822.

[74] L. Kong, X. Yin, X. Yuan, Y. Zhang, X. Liu, L. Cheng, L. Zhang, Electromagnetic wave absorption properties of graphene modified with carbon nanotube/poly (dimethyl siloxane) composites, Carbon 73 (2014) 185–193.

[75] J. Guo, H. Song, H. Liu, C. Luo, Y. Ren, T. Ding, M.A. Khan, D.P. Young, X. Liu, X. Zhang, J. Kong, Polypyrrole-interface-functionalized nano-magnetite epoxy nanocomposites as electromagnetic wave absorber with enhanced flame retardancy, J. Mater. Chem. C 5 (2017) 5334–5344.

[76] Y. Zhang, L. Qian, W. Zhao, X. Li, X. Huang, X. Mai, Z. Wang, Q. Shao, X. Yan, Z. Guo, Highly efficient Fe-N-C nanoparticles modified porous graphene composites for oxygen reduction reaction, J. Electrochem. Soc. 165 (2018) H510–H516.

[77] T. Su, Q. Shao, Z. Qin, Z. Guo, Z. Wu, Role of interfaces in two-dimensional photocatalyst for water splitting, ACS Catal. 8 (2018) 2253–2276.

[78] Q. Hou, J. Ren, H. Chen, P. Yang, Q. Shao, M. Zhao, X. Zhao, H. He, N. Wang, Q. Luo, Z. Guo, Synergistic hematite-fullerene electron extracting layers for improved efficiency and stability in perovskite solar cells, ChemElectroChem 5 (2018) 726–731.

[79] H. Du, C. Zhao, J. Lin, Z. Hu, Q. Shao, J. Guo, B. Wang, D. Pan, E.K. Wujick, Z. Guo, Carbon nanomaterials in direct liquid fuel cells, Chem. Rec. 18 (2018) 1365–1372.

[80] Q. Luo, H. Ma, Q. Hou, Y. Li, J. Ren, X. Dai, Z. Yao, Y. Zhou, L. Xiang, H. Du, H. He, All-carbon-electrode-based endurable flexible perovskite solar cells, Adv. Funct. Mater. 28 (2018) 1706777.

[81] W. Deng, T. Kang, H. Liu, J. Zhang, N. Wang, N. Lu, Y. Ma, A. Umar, Z. Guo, et al., Potassium hydroxide activated and nitrogen doped graphene with enhanced supercapacitive behavior, Sci. Adv. Mater. 10 (2018) 937–949.

[82] Y. Ma, L. Lv, Y. Guo, Y. Fu, Q. Shao, T. Wu, S. Guo, K. Sun, X. Guo, E.K. Wujick, Z. Guo, Porous lignin based poly (acrylic acid)/organo-montmorillonite nanocomposites: swelling behaviors and rapid removal of Pb (II) ions, Polymer 128 (2017) 12–23.

[83] M. Idrees, S. Batool, H. Ullah, Q. Hussain, M.I. Al-Wabel, M. Ahmad, A. Hussain, M. Riaz, Y.S. Ok, J. Kong, Adsorption and thermodynamic mechanisms of manganese removal from aqueous media by biowaste-derived

biochars, J. Mol. Liq. 266 (2018) 373–380.

[84] K. Gong, Q. Hu, L. Yao, M. Li, D. Sun, Q. Shao, B. Qiu, Z. Guo, Ultrasonic pre-treated sludge derived stable magnetic active carbon for Cr(VI) removal from wastewater, ACS Sustain. Chem. Eng. 6 (2018) 7283–7291.

[85] M. Idrees, S. Batool, T. Kalsoom, S. Yasmeen, A. Kalsoom, S. Raina, Q. Zhuang, J. Kong, Animal manure-derived biochars produced via fast pyrolysis for the removal of divalent copper from aqueous media, J. Environ. Manag. 213 (2018) 109–118.

[86] K. Gong, Q. Hu, Y. Xiao, X. Cheng, H. Liu, N. Wang, B. Qiu, Z. Guo, Triple layered core-shell ZVI@carbon@polyaniline composites enhanced electron utilization in Cr(VI) reduction, J. Mater. Chem. A 6 (2018) 11119–11128.

[87] S. Batool, M. Idrees, Q. Hussain, J. Kong, Adsorption of copper (II) by using derived-farmyard and poultry manure biochars: efficiency and mechanism, Chem. Phys. Lett. 689 (2017) 190–198.

[88] S. Batool, M. Idrees, M.I. Al-Wabel, M. Ahmad, K. Hina, H. Ullah, L. Cui, Q. Hussain, Sorption of Cr(III) from aqueous media via naturally functional-ized microporous biochar: mechanistic study, Microchem. J. 144 (2019) 242–253.

[89] Y. Li, T. Jing, G. Xu, J. Tian, M. Dong, Q. Shao, B. Wang, Z. Wang, Y. Zheng, C. Yang, Z. Guo, 3-D magnetic graphene oxide-magnetite poly (vinyl alcohol) nanocomposite substrates for immobilizing enzyme, Polymer 149 (2018) 13–22.

[90] X. Cui, G. Zhu, Y. Pan, Q. Shao, M. Dong, Y. Zhang, Z. Guo, Poly-dimethylsiloxane-titania nanocomposite coating: fabrication and corrosion resistance, Polymer 138 (2018) 203–210.

[91] Y. He, S. Yang, H. Liu, Q. Shao, Q. Chen, C. Lu, Y. Jiang, C. Liu, Z. Guo, Reinforced carbon fiber laminates with oriented carbon nanotube epoxy nano-composites: magnetic field assisted alignment and cryogenic temperature mechanical properties, J. Colloid Interface Sci. 517 (2018) 40–51.

[92] Z. Hu, D. Zhang, F. Lu, W. Yuan, X. Xu, Q. Zhang, H. Liu, Q. Shao, Z. Guo, Y. Huang, Multistimuli-responsive intrinsic self-healing epoxy resin con-structed by host–guest interactions, Macromolecules 51 (2018) 5294–5303.

[93] Y. Lu, M.C. Biswas, Z. Guo, J.W. Jeon, E.K. Wujcik, Recent developments in bio-monitoring via advanced polymer nanocomposite-based wearable strain sensors, Biosens. Bioelectron. 123 (2019) 167–177.

[94] Z. Hu, Q. Shao, Y. Huang, L. Yu, D. Zhang, X. Xu, J. Lin, H. Liu, Z. Guo, Light triggered interfacial damage self-healing of poly (p-phenylene benzobisox-azole) fiber composites, Nanotechnology 29 (2018) 185602.

[95] Z. Li, B. Wang, X. Qin, Y. Wang, C. Liu, Q. Shao, N. Wang, J. Zhang, Z. Wang, C. Shen, Z. Guo, Superhydrophobic/superoleophilic polycarbonate/carbon nanotubes porous monolith for selective oil adsorption from water, ACS Sustain. Chem. Eng. 6 (2018) 13747–13755.

[96] B. Song, T. Wang, H. Sun, H. Liu, X. Mai, X. Wang, L. Wang, N. Wang, Y. Huang, Z. Guo, Graphitic carbon nitride (g-C$_3$N$_4$) Interfacially Strengthened carbon fiber epoxy composites, Compos. Sci. Technol. 167 (2018) 515–521.

[97] B. Zhou, Y. Li, K. Dai, G. Zheng, C. Liu, Y. Ma, J.X. Zhang, N. Wang, C. Shen, Z. Guo, Continuously fabricated transparent conductive polycarbonate/car-bon nanotube nanocomposite film for switchable thermochromic applica-tions, J. Mater. Chem. C 6 (2018) 8360–8371.

[98] Z. Hu, Q. Shao, M.G. Moloney, X. Xu, D. Zhang, J. Li, C. Zhang, Y. Huang, Nondestructive functionalization of graphene by surface-initiated atom transfer radical polymerization: an ideal nanofiller for poly (p-phenylene benzobisoxazole) fibers, Macromolecules 50 (2017) 1422–1429.

[99] J. Li, S. Ge, J. Wang, H. Du, K. Song, Z. Fei, Q. Shao, Z. Guo, Water-based rust converter and its polymer composites for surface anticorrosion, Colloids Surf. A 537 (2018) 334–342.

[100] Z. Hu, Q. Shao, X. Xu, D. Zhang, Y. Huang, Surface initiated grafting of polymer chains on carbon nanotubes via one-step cycloaddition of diary-lcarbene, Compos. Sci. Technol. 142 (2017) 294–301.